BAROCLINIC WAVES IN THE MARTIAN ATMOSPHERE: STUDY USING THE CCSR/NIES MARTIAN GCM

Takeshi Kuroda, *Max-Planck-Institute for Solar System Research, Katlenburg-Lindau, Germany (kuroda@mps.mpg.de)*, **Masaaki Takahashi**, *Center for Climate System Research, University of Tokyo, Japan.*

Introduction: We present the results of simulations with a recently developed Martian General Circulation Model (GCM) which are consistent with observations by spacecrafts and landers. We analyze the origin of the thermal structures and atmospheric waves. Using the consistent time- and latitude-dependent dust scenarios prescribed externally, the CCSR/NIES Martian GCM can reproduce temperature distributions and seasonal variance of the surface pressure, and atmospheric waves which seem to be baroclinic in the northern midlatitudes from autumn to spring. These waves have periods of more than 1 Sol. The model reproduces the significant reduction in wave activity when the dust opacity is very high, as observed by the Viking Landers in 1977 [*Kuroda et al*., 2005]. In this presentation we present the outline of the CCSR/NIES Martian GCM, and show the results of simulations. We also present the analyses of the waves in northern autumn and winter midlatitudes, to show the changes in the atmospheric structures owing to the global dust storm.

Model Description: The Martian GCM used in this study is based on CCSR/NIES AGCM, a terrestrial atmospheric model based on three-dimensional primitive equations with spectral transformation method in horizontal and sigma coordinate in vertical [*Numaguti et al*., 1997]. The horizontal resolution is set at about 5.6° latitude by 5.6° longitude (triangular truncation with truncation T21). The vertical resolution is 33 layers up to the height of about 80 km. Rayleigh friction is imposed near the upper boundary, with the damping time of 1/10 Sol at the top of the model. Topography, albedo and thermal inertia data for Mars surface are introduced.

As for the radiative processes, the effects of CO_2 and dust suspended in the atmosphere are considered. The absorption and emission of infrared radiation at CO_2 15 μm and 4.3 μm bands are calculated using the *k*-distribution method [*Nakajima and Tanaka*, 1986]. The atmospheric heating due to absorption of solar radiation in CO_2 near-infrared bands is also included using the simple analytical formula used by *Forget et al.* [1999].

The absorption, emission and scattering by the atmospheric dust are calculated using the two-stream discrete-ordinate/adding method [*Nakajima and Tanaka*, 1986]. The dust radiation scheme utilizes 19 representative wavelength bands: 9 in the visible (0.2~4 μm) and 10 in the infrared (4~1000 μm) spectral range. The corresponding radiative fluxes depend on the dust parameters, the refractive indices and the particle size distribution. The refractive indices of the dust for the visible wavelengths (shorter than 5 μm) are taken from *Ockert-Bell et al.* [1997], the montmorillonite 219b data of *Toon et al.* [1977] are employed for the wavelengths between 5 and 17 μm, and constant values of *Forget* [1998] are utilized for the wavelengths longer than 17 μm. The dust particle size distribution is borrowed from *Tomasko et al.* [1999], using the modified gamma function with the effective radius of 1.6 μm and the effective variance of 0.2 μm. In the 15 μm and 4.3 μm bands which CO_2 absorption band exists, the optical depth of CO_2 and dust are added to calculate the radiative fluxes.

Atmospheric dust distributions are consistent with the time- and latitude-dependent dust opacity distributions observed by Mars-orbiting spacecrafts. Here we introduce the analytical functions to define the TES2 and VIK1 dust scenarios, made to correspond to the observations by MGS-TES in 1999 and Viking spacecraft in 1977, respectively. First, the variances of dust opacity depending on the aerocentric longitude L_s are expressed by the following formulas:

$$\tau_*(L_s) = 0.05 + \frac{\tau_{\max} - 0.05}{2}\left[1 + \tanh\{(L_s - L_{s0})\alpha\}\right]$$
$$\text{for } L_s < L_{s1},$$
$$\tau_*(L_s) = 0.05 + (\tau_{\max} - 0.05)\{\cos((L_s - L_{s1})/2)\}^{\beta}$$
$$\text{for } L_s \geq L_{s1}, \qquad (1)$$

where $\tau_*(L_s)$ denotes the infrared (9~10 μm) dust opacity at 7 hPa calculated at the equator, south and north poles, as τ_{eq}, τ_S and τ_N, respectively. The factor τ_{max} is the maximum opacity in each region, L_{s0} is the aerocentric longitude at the time of the most intense dust storm, L_{s1} is the aerocentric longitude for the time when the dust opacity begins to decrease, and α and β are the rates of the opacity increase and decrease, correspondingly. These factors are presented in Table 1. The optical depth at all latitudes ϕ, $\tau_*(\phi, L_s)$, is then prescribed as follows.

$$\tau(\phi, L_s) = \tau_N + \frac{\tau_{eq} - \tau_N}{2}\left\{1 + \tanh\left[5\left(45^\circ - \phi\right)\right]\right\}$$
$$\text{for } \phi > 0,$$

	TES2			VIK1(1)			VIK1(2)		
	N	EQ	S	N	EQ	S	N	EQ	S
τ_{max}	0.1	0.2	0.5	0.1	0.6	0.8	0.2	1.3	1.5
L_{s0}	225°	220°	215°	216°	206°	206°	280°	272°	272°
L_{s1}	240°	235°	235°	230°	215°	218°	295°	283°	283°
α	12	15	8	12	22	22	12	18	18
β	30	30	20	30	10	10	30	23	23

Table 1: Values of the factors used in formulas (1)~(3) for deciding time-latitude profiles of three dust scenarios used in this paper. N, EQ and S correspond to the factors for calculating τ_N, τ_{eq} and τ_S, respectively. In VIK1 dust scenario two major dust storms occur, so the optical depth τ is defined by $\tau=\max[\tau_1,\tau_2]$, where τ_1 and τ_2 are the optical depths of VIK1(1) and VIK1(2), respectively, in the table.

$$\tau(\phi, L_s) = \tau_S + \frac{\tau_{eq} - \tau_S}{2}\left\{1 + \sin\left[2\left(45^\circ + \phi\right)\right]\right\} \quad \text{for } \phi<0. \qquad (2)$$

The vertical distribution of the dust mixing ratio Q is given by the formulas adopted by *Forget et al.* [1999] and *Lewis et al.* [1999], defining the cut-off altitude of the dust [km], z_{max}, with the opacity instead of the aerocentric longitude:

$$Q = Q_0 \exp\left\{0.007\left[1 - \left(\frac{p_0}{p}\right)^{70/z_{\max}}\right]\right\},$$

$$z_{\max}(\phi, L_s) = 80 - 8(\tau - 2)^2 - 11\sin^2\phi, \qquad (3)$$

where p is the pressure, p_0 is the standard pressure (7 hPa), and Q and Q_0 are the dust mixing ratio at the levels p and p_0, respectively. The time-latitude profiles of each dust scenario are shown in Figure 1.

The thermal effects and atmospheric mass change owing to CO_2 condensation and sublimation are included, in the same way as *Forget et al.* [1998]. When the atmospheric temperature predicted from dynamical and physical processes is below the condensation temperature, the condensation occurs and the condensed CO_2 falls to the surface immediately. Then the latent heat released by the condensation, the potential energy released by ice falling and the energy used to heat the ice to the condensation temperature of lower level are taken into account in the thermal effects. The surface pressure is adjusted to conserve the total mass of CO_2 (caps + atmosphere). The change of the surface albedo associated with polar cap formation is also included.

Model results: Figure 2 shows the simulated zonal-mean temperature in the model with the TES2 dust scenario at northern winter solstice. This figure shows a good consistency with MGS-TES observation at the same season shown in *Smith et al.* [2001]. Figure 3 presents the mass stream function at the same season. This figure shows a good agreement with the results in other GCMs [*Haberle et al.*, 1993;

(a) TES2 dust scenario

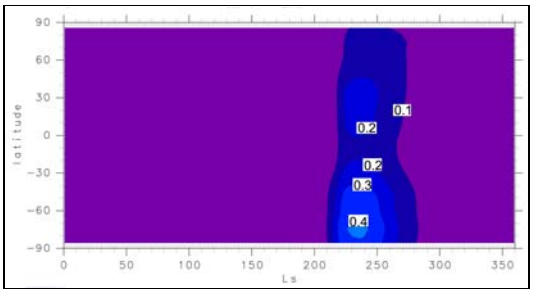

(b) VIK1 dust scenario

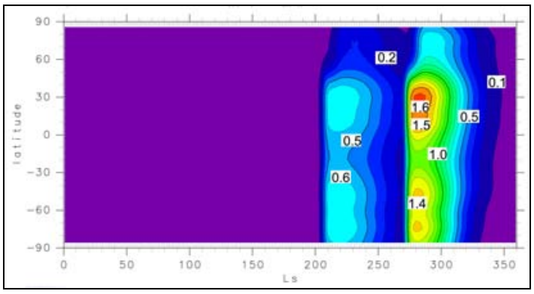

Figure 1: Time-latitude profiles of the zonal-mean dust optical depth in infrared wavelength (9-10 µm) at surface in the (a) TES2 and (b) VIK1 dust scenar-

ios.

Forget et al., 1999; *Richardson and Wilson*, 2002; *Takahashi et al.*, 2003]. Ferrell circulation is seen in this figure in northern mid- and high-latitude, which should indicate the existence of baroclinic waves there.

Figure 4 shows the annual variation of the surface pressure at the nearest grid of Viking Lander 1 and 2, along with the observational data of Viking Landers for comparison. The results are in good agreement between the model and observations if the VIK1 dust scenario is used, with the maximum synoptic difference of ~0.3 hPa. The significant reduction of synoptic period oscillations in L_s=280°~310°, during the second planet-encircling dust storm, is also reproduced. In the model results with the TES2 dust scenario this reduction is not seen, as also shown in Figure 4, so it is predictable that the global dust storm soon after the winter solstice suppresses the waves.

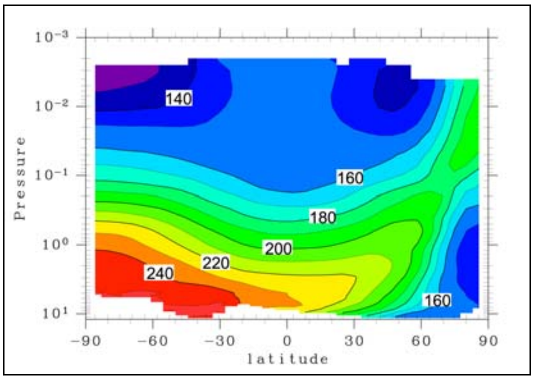

Figure 2: Numerical results of time- and zonal-mean atmospheric temperature [K] at northern winter solstice (L_s=265°-275°) in the model with the TES2 dust scenario.

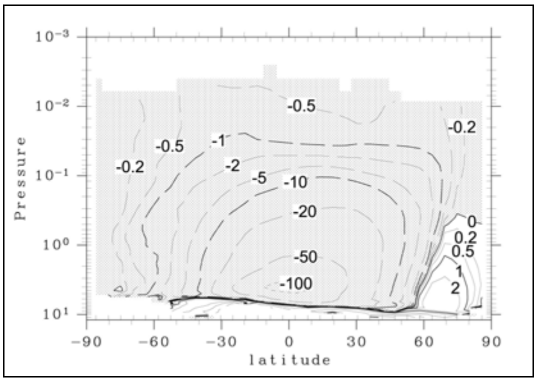

Figure 3: Same as Figure 2, except for mass stream function [10^8 kg s^{-1}].

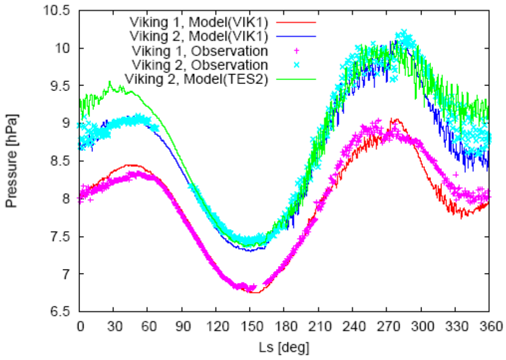

Figure 4: Seasonal variation of daily-averaged surface pressure [hPa]. Red and blue lines show the model results with the VIK1 dust scenario at the nearest grid point of Viking Lander 1 and 2, respectively. Magenta pluses and cyan crosses show the observational results by Viking Landers 1 and 2, respectively. Green line shows the model results with the TES2 dust scenario at the nearest grid point of Viking Lander 2.

Baroclinic waves: The oscillations seen in Figure 4 from autumn to winter indicate the existence of atmospheric waves with periods >1 Sol. Spectral analyses show the peaks with the period of 6.6 and 3.2 Sols in both models (with the TES2 and VIK1 dust scenario, respectively) at Ls=210°~250°, as shown in Figure 5(a). A small peak with the period 2.4 Sols is also seen in the model with the TES2 dust scenario, and these periods are consistent with the "fall spectra" in *Barnes* [1980] from the observational data by Viking Lander 2. These periods seem to correspond to the waves with the zonal wavenumber 1 (6.6 Sols), 2 (3.2 Sols) and 3 (2.4 Sols) as far as seeing the longitude distribution of synoptic daily-averaged geopotential height deviation in midlatitude when each wave is dominant. This is consistent with the analyses of MGS-TES data [*Wilson et al.*, 2002] which showed a dominant eastward propagating wave with the zonal wavenumber 1 and 6.5 Sols period. Figure 6 shows the longitude-height distribution of the geopotential height deviation when the wave with the period of 3.2 Sols is dominant. This figure shows the structure of the zonal wavenumber 2, tilted troughs and ridges to west as elevating, vertical warm/cold axes which exist on the troughs/ridges near the surface and on the eastward ridges/troughs around the height of 1 hPa. This is similar to the synoptic disturbance due to baroclinic waves [e.g. *Holton*, 1992].

At Ls=280°~300°, during the second global dust storm, the model results with the VIK1 dust scenario show only a small peak with the period of 5.5 Sols, while those with the TES2 dust scenario show two dominant peaks with the period of 5.5 and 2.5 Sols, as shown in Figure 5(b). The periods dominant in the model results with the TES2 dust scenario seem to correspond to the zonal wavenumber of 1 (5.5 Sols) and 2 (2.5 Sols), which is consistent with the model study by *Collins et al.* [1996]. By contrast, in the model results with the VIK1 dust scenario the wavenumber of the wave with the period of 5.5 Sols seem to be more than 1. This indicates that phase speeds decrease significantly owing to the global dust storm, as shown in *Barnes* [1980]. In the presentation we are going to present more analyses of the model results with each dust scenario in this time, to see the effects of the global dust storm on the change of the wave characteristics.

References: Kuroda T. et al., *J. Meteorol. Soc. Japan 83*, 1-19, 2005; Numaguti A. et al., *CGER's Supercomputer Monograph Report Vol.3*, 1-48, 1997; Nakajima T. and M. Tanaka*, J. Quant. Spectrosc. Radiat. Transfer 35*, 13-21, 1986; Forget F. et al., *J. Geophys. Res. 104*, 24155-24175, 1999; Ockert-Bell M. E. et al., *J. Geophys. Res. 102*, 9039-9050, 1997; Toon O. B. et al., *Icarus 30*, 663-696, 1977; Forget F., *Geophys. Res. Lett. 25*, 1105-1108, 1998; Tomasko M. G. et al., *J. Geophys. Res. 104*, 8987-9007, 1999; Lewis S. R. et al., *J. Geophys. Res. 104*, 24177-24194, 1999; Forget F. et al., *Icarus 131*, 302-316, 1998; Smith M. D. et al., *J. Geophys. Res106*, 23929-23945, 2001; Haberle R. M. et al. *J. Geophys. Res. 98*, 3093-3124, 1993; Richardson M. I. and R. J. Wilson, *Nature 416*, 298-301, 2002; Takahashi Y. O. et al., *J. Geophys. Res. 108(E3)*, 10.1029/2001JE001638, 2003; Barnes J. R., *J. Atmos. Sci. 35*, 723-734, 1980; Wilson R. J. et al., *Geophys. Res. Lett. 29*, 10.1029/2002GL014866, 2002; Holton J. R., *An Introduction to Dynamic Meteorology, Academic Press*, 1992; Collins M. et al., *Icarus 120*, 344-357, 1996.

(a) Surface pressure spectra at L_s=210°~250°

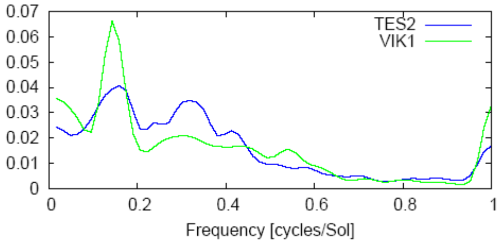

(b) Surface pressure spectra at L_s=280°~300°

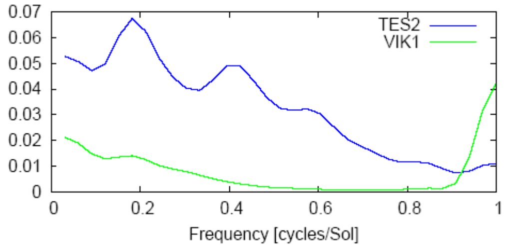

Figure 5: Power spectra of surface pressure at the nearest grid point of Viking Lander 2 in the models with the TES2 and VIK1 dust scenarios. The periods analyzed are (a) L_s=210°~250° (between the onsets of two global dust storms in the VIK1 dust scenario) and (b) L_s=280°~300° (soon after the onset of the second global dust storms in the VIK1 dust scenario, when the significant reduction of synoptic period oscillations is seen).

(a) Geopotential height

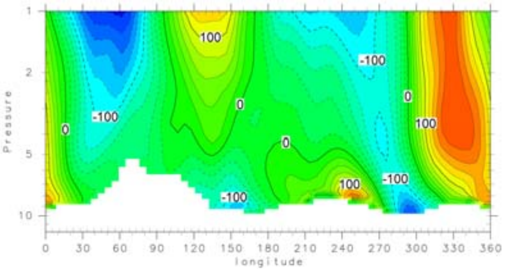

(b) Temperature

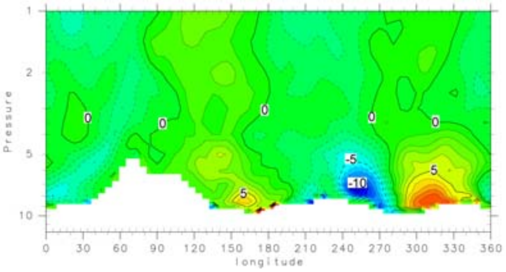

Figure 6: Longitude-height distributions of the deviations of daily-averaged (a) geopotential height and (b) temperature at the latitude of 47° N (the same latitude as the nearest grid point of Viking Lander 2) up to the height of 1 hPa when the wave with the period of 3.2 Sols is dominant in the model with the TES2 dust scenario (L_s~215°).